ACS NANO

ARTICLE

Cite This: ACS Nano 2019, 13, 12798−12809

www.acsnano.org

Plug-In Safe-by-Design Nanoinorganic Antibacterials

Milan Gautam,[†,‖] Dae Hoon Park,[‡,‖] Sung Jae Park,[‡] Kang Sik Nam,[‡] Geun Young Park,[‡] Jungho Hwang,[*,‡] Chul Soon Yong,[†] Jong Oh Kim,[*,†] and Jeong Hoon Byeon[*,§]

[†]College of Pharmacy, Yeungnam University, Gyeongsan 38541, Republic of Korea
[‡]School of Mechanical Engineering, Yonsei University, Seoul 03722, Republic of Korea
[§]School of Mechanical Engineering, Yeungnam University, Gyeongsan 38541, Republic of Korea

Supporting Information

ABSTRACT: Due to antimicrobial resistance and the adverse health effects that follow broad and inappropriate use of antibacterial agents, new classes of antibacterials with broad and strong bactericidal activity and safety for human use are urgently required globally, increasingly so with the onset of climate change. However, R&D in this field is known to be rarely profitable, unless a cost-effective, flexible, and convenient platform that ensures the production of workable candidate antibacterials can be developed. To address this issue, inorganic nanomaterials have been considered for their bactericidal activities, yet further investigations of composition crystalline modifications and/or surface biomaterial coatings are still required to provide effective and safe antibacterial nanoparticles. In this study, we developed a plug-in system comprising a spark plasma reactor and a flow heater under nitrogen gas flow to supply precursor inorganic nanoparticles (Cu−Te configuration) that can be modulated in-flight at different temperatures. From antibacterial and toxicological assays in both *in vitro* and *in vivo* models, bactericidal and toxicological profiles showed that the plug-in system-based platform can be used to identify key parameters for producing safe-by-design agents with antibacterial activity [>88% (*in vitro*) and >80% (*in vivo*) in antibacterial efficiency] and safety (>65% in *in vitro* viability and >60% in *in vivo* survival rate).

KEYWORDS: antimicrobial resistance, antibacterial agents, inorganic nanomaterials, plug-in system, safe-by-design antibacterials
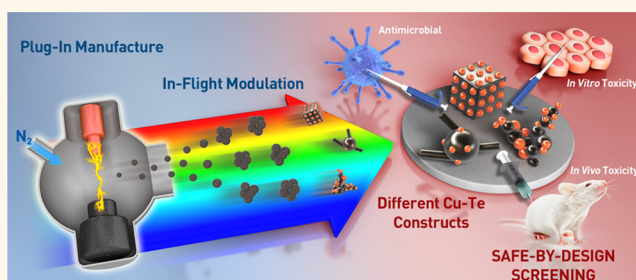
Antibacterial agents with broad-spectrum activity have long (approximately 90 years) been sought for medical and hygiene applications, and various antibacterial formulations and coatings have been widely used to suppress or abolish bacterial growth in bioindustrial and biomedical fields.[1] However, the broad and inappropriate use of such agents is followed by antimicrobial resistance (AMR) to the formulations and coatings. This is an urgent global health and environmental problem, particularly in the wake of climate change.[2−4] Moreover, inappropriate use of antibacterials can lead to side reactions and intolerable toxicity.[5] The urgency of issues relating to AMR has motivated estimates of the associated socioeconomic costs, and it is clear that more innovative approaches are required to provide efficacious antibacterial agents with broad-spectrum activities and efficient production processes. R&D into antibacterials is rarely profitable because timely realization of new agents is hampered by requirements of expensive biosafety assessments and clinical trials.[6−8] Polymeric antibacterial nanosystems and their related synthetic approaches have been introduced recently as alternative approaches to AMR, but many important challenges
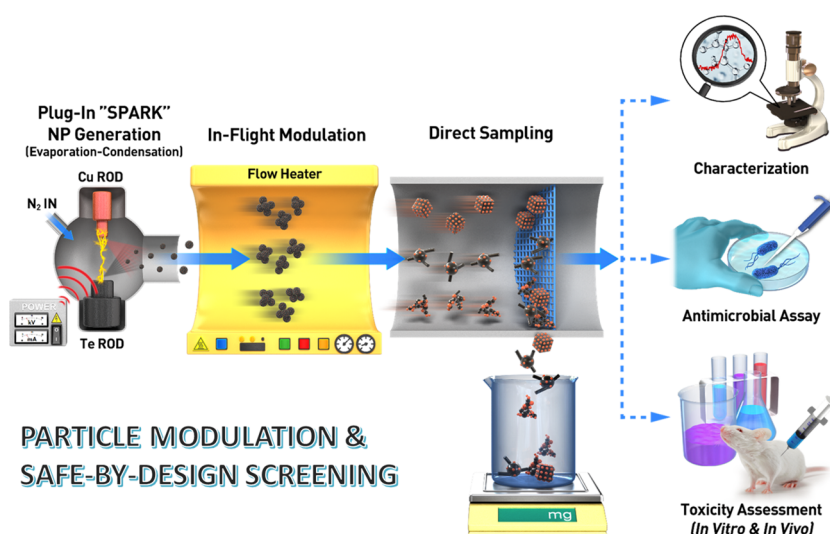
remain in the optimization of antibacterial agents, which are required to have broad-spectrum activity, cost-effective production processes, antibacterial mechanisms, defined metabolic pathway effects and toxicity profiles,[9] and demonstrably limited impacts on the environment.[10] Moreover, the procedures for preparation, storage, and validation of candidate materials are based on traditional multistep chemical processes and purifications,[11,12] which may not be conducive to timely realization through rapid screening of candidate materials.

Because of their qualified broad-spectrum activity and cost-effectiveness, nanoinorganic antibacterials have been increasingly studied in recent years.[13] Inorganic nanomaterials have been shown to damage bacteria through reactive oxygen species (ROS) generation and physical injury following disturbed enzyme activity, DNA synthesis, and energy transduction. These agents have low acute toxicity and long-term stability[2,3] but can be toxic above certain concentration thresholds. To improve

Accepted: November 5, 2019
Published: November 5, 2019

Downloaded via YONSEI UNIV on November 26, 2019 at 13:43:55 (UTC).
See https://pubs.acs.org/sharingguidelines for options on how to legitimately share published articles.

ACS Publications   © 2019 American Chemical Society   **12798**   DOI: 10.1021/acsnano.9b04939
ACS Nano 2019, 13, 12798−12809

Figure 1. Schematic of the procedure for modulating and directly collecting Cu−Te constructs for antibacterial and toxicological assays; two serially connected plug-in devices, a spark plasma reactor, and a flow heater were used to conveniently supply precursor Cu−Te NPs and treat them with wall temperatures (RT, 400 °C, or 800 °C) in a single-pass manner. The evaporation−condensation of Cu and Te rods from atmospheric spark ablation under a nitrogen gas flow produced precursor Cu−Te NPs, which were then injected into the flow heater. Control of the wall temperature of the heater induced changes in the pore phase of NPs, resulting in the formation of different Cu−Te constructs (dendrites, spikes, or cubes) during a residence time of less than 5 s. Changes in antibacterial activity and biocompatibility were examined after directly dispersing Cu−Te constructs in buffered saline. Antibacterial (including MDR strains), *in vitro* (human dermal fibroblast HDF and human fetal lung fibroblast WI-38 cells), and *in vivo* (ICR mice) toxicological assays were performed to ensure the production of safe-by-design nanoinorganic antibacterials within 3 weeks.

toxicity profiles, compositional/crystalline modifications and/or biophilic surface treatments have been employed to ensure effective antibacterial activities with minimal toxicities. To this end, green compound mediated or biogenic synthesis of nanoinorganic antibacterials has been introduced. These environmentally compatible compounds or bacteria are used as reducing agents for inorganic ions and lead to the formation of zerovalent nanoinorganic constructs.[14−17] These approaches, however, require multiple hydrothermal reactions and separation procedures and only provide case specific information, offering limited coverage as platforms for efficient screening of optimal nanoinorganic antibacterials. Hence, this approach may fail to resolve the circumstantial limitations of R&D efforts for antibacterials.[6] A convenient, fast, and flexible platform for rapidly screening candidate materials may be an essential prerequisite for the use of inorganic nanomaterials as antibacterials.

To this end, we designed a plug-in system (Figure S1A) for on-demand single-pass production of inorganic nanomaterials using constructs that influence antibacterial activities according to the resulting surface properties and bacteria-binding properties.[18] Nanoparticles (NPs) generated using this system can be conveniently applied to antibacterial and toxicological assays, and the resulting data are used to ensure rapid production of safe-by-design antibacterials. A spark plasma reactor and a flow heater were serially connected to supply inorganic precursor NPs and subsequently modulate their properties by sintering them in-flight. Spark plasma was selected as the precursor (Cu−Te in this study) NP supply because it can be used widely to ablate most conductive materials in a plug-in configuration without the use of hydrothermal chemistries and post-treatments.[19] Specifically, spark-plasma-based systems recently introduced the fabrication of both NPs (Ag, Cu, Zn, or Mg) and NP composites (Cu−Ag) in a plug-in manner under ambient conditions.[20,21] Changes in size distributions of the NP supply

before entering the flow heater can be calculated using the following equation:[22]

$$\frac{dN_i}{dt} = -\frac{dC_{vap}}{dt} - \left\{ N_i \sum_{j=1}^{n} \beta_{i,j} N_j \right\} \rho_g \tag{1}$$

where N_i and N_j are the number concentrations of singlet (primary) and agglomerate (from Brownian motion) particles, respectively, $\beta_{i,j}$ is the collision kernel between i and j components, and ρ_g is the gas density. The concentration of vaporized inorganic components (C_{vap}) can be estimated using the following equation:[23]

$$C_{vap} = \frac{p_v M_v}{p_v M_v + (p_{atm} - p_v) M_g} \tag{2}$$

where p_v and p_{atm} are partial vapor and atmospheric pressures, respectively, and M_v and M_g are the molecular weights of the vapor and the gas, respectively. The spark ablation temperature is calculated as $T_{spark} \sim \left(\frac{E_{spark}}{C_v v_{spark} \rho_g} \right) + T_g$, where E_{spark} is the spark ablation energy, C_v is the specific heat at constant volume, v_{spark} is the volume of the spark channel, and T_g is the gas temperature.[24] Another plug-in modulation to build different Cu−Te constructs through in-flight sintering was attempted by injecting precursor NPs into the electrically operated flow heater. Changes in the pore phase (P_{pore}) of the NPs at different temperatures can induce assembly of different Cu−Te constructs within 5 s and can be modulated according to the following equation:[25]

$$\frac{dP_{pore}}{dt} = \frac{cD\gamma a_0^3}{l^3 k_B T} \tag{3}$$
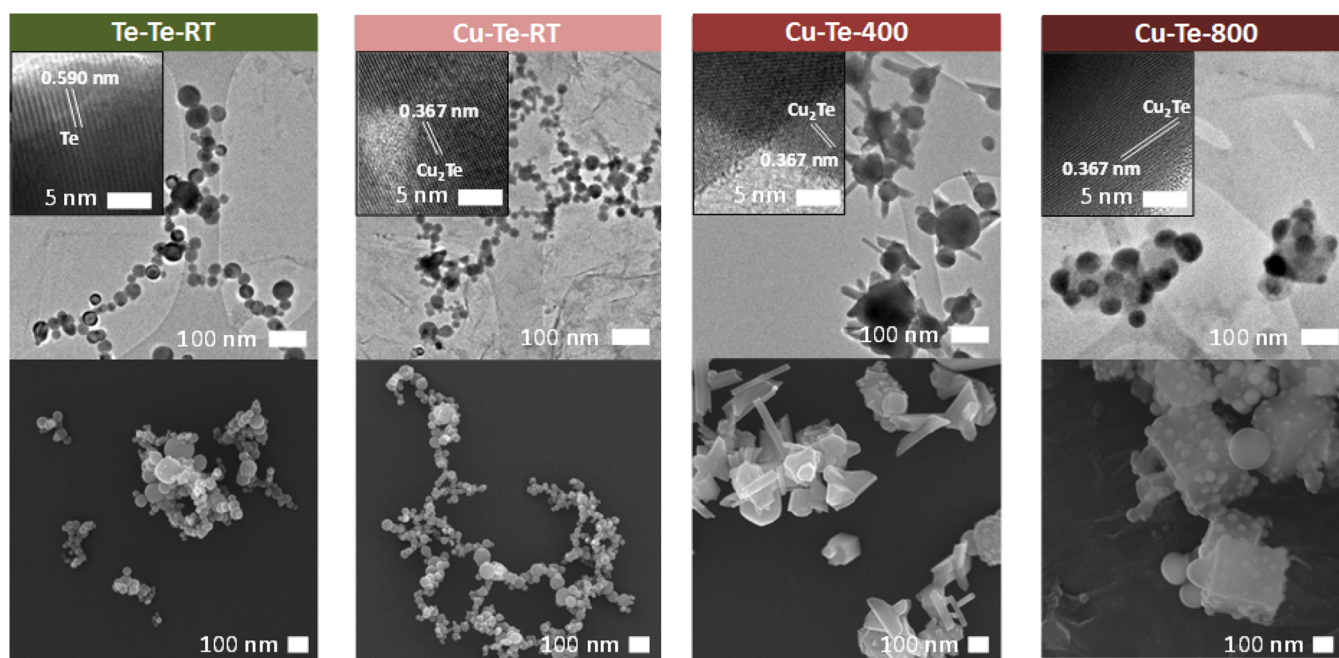
Figure 2. Tandem electron microscopy (TEM) and scanning electron microscopy (SEM) observations of Cu−Te constructs; Cu−Te constructs from the plug-in system were directly deposited on lacey carbon-coated Cu grids to obtain low- and high-magnification TEM images. Constructs were collected on ultraflat Si wafers for SEM observations. Both observations show that Cu−Te NPs can be altered in single-pass reactions. Insets of TEM images exhibit alloying of Cu and Te elements in microstructures of individual Te particles at room temperature (RT).

where c is the constant relevant to the pore phase, D is the diffusion coefficient, γ is the surface energy, a_0 is the lattice spacing, l is the size of a singlet particle, k_B is the Boltzmann constant, and T is the operation temperature. Using these modulations, we prepared three different Cu−Te constructs (dendrites, spikes, and cubes) at room temperature (RT), 400 °C, or 800 °C and named these Cu−Te−RT, Cu−Te−400, and Cu−Te−800, respectively. Prior to antibacterial and toxicological assays, constructs were directly dispersed in buffered saline, as shown in Figure 1. Cu−Te NPs were selected because the ions Cu^{2+}, TeO_3^{2-}, and TeO_4^{2-} are released from the constructs and are highly toxic to bacteria because they interact with and deactivate bacterial proteins.[26−30] Whereas Cu is an essential micronutrient for human health, Te (chemically similar to other chalcogens) exhibits no significant toxicities in mammalian cells and has no unfavorable excretion properties in human trials.[31−35] Furthermore, the Cu−Te combination may combine the weak antibacterial activity of Te toward Gram-positive strains[30,36] with the toxicity of Cu beyond a certain concentration.[37] Recently, nanoinorganic Te has also been used to treat cancer and Parkinson's disease because of its excellent biocompatibility and physicochemical properties.[38−40] In antibacterial assays, minimum inhibitory concentrations (MIC) and antibacterial efficiency were examined following Cu−Te exposures of Gram-negative (*Escherichia coli*) and positive (*Staphylococcus epidermidis*) bacteria. These multidrug-resistant (MDR) bacteria included extended-spectrum β-lactamase (ESBL)-producing *E. coli* and methicillin-resistant *S. aureus* (MRSA) strains. As *in vitro* toxicity assessments, we performed 3-(4,5-dimethylthiazole-2-yl)-2,5-diphenyltetrazolium bromide (MTT) and dichloro-dihydro-fluorescein diacetate (DCFH-DA) assays to determine cell viability and ROS generation, respectively, after treating human dermal fibroblast (HDF) and human fetal lung fibroblast (WI-38) cells with Cu−Te constructs for 24 or 48 h. *In vivo* toxicity was assessed following intraperitoneal injections of the constructs into Institute of Cancer Research mice. These mice can be used to obtain reproductive information from toxicological assays.[41] A high single dose of 100 mg kg^{-1} was selected for histopathological, hematological, and biochemical analyses, which were performed within 3 weeks (18 days in this study) of treatments.

RESULTS AND DISCUSSION

Equations 1 and 2 accommodate the much greater diffusion coefficient of Cu−Te NPs in the gas phase than in the aqueous phase.[42] Size distributions of Cu−Te constructs from different operating conditions were converged and returned nearly identical geometric mean diameters and geometric standard deviations of less than 200 nm and 1.8, respectively (Figure S1B). The average total number concentration of NPs was approximately 1.8×10^7 particles cm^{-3}, and no significant differences were observed between the plug-in operations. These data show that the developed plug-in system produces comparable size distributions of different constructs, thus ensuring relevance of comparisons. Data from scanning electron microscopy−energy dispersive X-ray spectroscopy (SEM−EDS) analyses of particles that were collected directly in-flight on ultraflat substrates are depicted in Figure S2A. To generate representative results, EDS mapping was conducted on the particle film (left SEM images). Both Cu and Te elements were clearly observed in all Cu−Te constructs, and the resulting elemental ratio between Cu and Te was approximately 1:9. This value reflects significant differences in the heat of vaporization parameters of Cu (300.30 kJ mol^{-1}) and Te (52.55 kJ mol^{-1}). Thus, the plug-in system provided an appropriate imbalance for tuning Cu fractions in favor of enhancing the antibacterial activity of Te toward Gram-positive bacteria and exploiting the low toxicity of Te. This elemental imbalance was further confirmed using Raman spectroscopy analyses (Figure S2B). Compared with the individual Te profile, no other observable

bands and/or shifts were found in Cu−Te constructs, thus proving the Te-dominant composition. Based on elemental analyses, total mass concentrations (bottom table in Figure S1) of the constructs were determined. The average mass production rate was estimated at about 0.15 g h^{-1}. These data suggest that the plug-in system can produce sufficient quantities of Cu−Te for *in vitro* and *in vivo* antibacterial and toxicological assays in only 20 min (about 0.05 g of each construct is required for whole bioassays). The plug-in modulability of shape and microstructure from in-flight sintering (eq 3) was examined using transmission electron microscopy (TEM) and SEM observations (Figure 2). Compared with Te−Te−RT, the construct Cu−Te−RT exhibited a clear dendritic structure of discontinuous channels (pores), with an effective fractal dimension [D_f] of about 1.8.[43] However, the constituent singlet particles were spherical in both constructs. High-magnification TEM images of Cu−Te−RT show *d*-spacings of 0.367 nm (hexagonal Cu$_2$Te phase),[44] but a *d*-spacing of 0.590 nm for Te−Te−RT (hexagonal Te plane),[45] suggesting partial alloying between Cu and Te components under the elemental imbalance that facilitates differing build-up modes. These alloyed Cu−Te regions were also observed in parts of Cu−Te−400 and Cu−Te−800 constructs, further indicating the elemental imbalance. Nonetheless, shapes of singlet particles constituting the Cu−Te−400 construct were transformed into a spiky structure with D_f values of about 2.2. These particles were further transformed into a cubic structure (Cu−Te−800) with a D_f value of 2.5 following increases in the operating temperature of the flow heater. Hence, we achieved thermal modulation of pore phases of the constructs, and these thermal properties were confirmed in X-ray diffractometry (XRD; Figure 3) analyses of the constructs. Stiffnesses and intensities of lattice planes of hexagonal Te (JCPDS 01-079-0736)[46] in Cu−Te−RT were enhanced at 400 °C (Cu−Te−400), and ratios of peak intensities $I_{(100)}/I_{(011)}$ and $I_{(012)}/I_{(110)}$ were also changed significantly at 800 °C (Cu−Te−800), likely reflecting changes
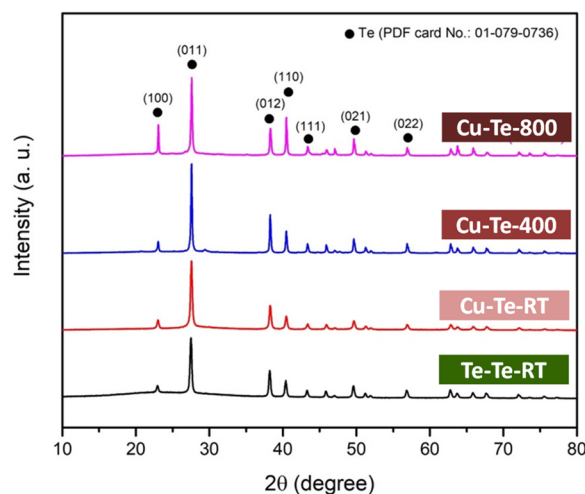
Figure 3. X-ray diffraction (XRD) profiles of Cu−Te constructs, including individual Te particles at RT; the weights of specimens were identical for all measurements, and the specimens clearly exhibited the characteristic bands of Te, representing a compositional imbalance between Cu and Te. No significant differences were observed between Te−Te−RT and Cu−Te−RT, whereas bands for Cu−Te alloys were clarified for Cu−Te−400 and Cu−Te−800 constructs (Figure S3).

in pore phases of the constructs. Furthermore, characteristic peaks of Cu−Te alloys (JCPDS 01-070-8050 and 00-043-1401) were observable in Cu−Te−400 and Cu−Te−800 constructs (Figure S3), suggesting that the alloyed parts protrude during in-flight sintering. Accordingly, TEM images show anisotropy of singlet particles of Cu−Te−400 and Cu−Te−800 constructs, which were detected easily in XRD measurements. Broader light absorbance profiles of Cu−Te−400 and Cu−Te−800 dispersions in phosphate-buffered saline compared with Cu−Te−RT also represent the relative anisotropy of the two constructs (Figure S4). X-ray photoelectron spectroscopy (XPS) analyses (Te 3d and Cu 2p) of the cores of Cu−Te constructs further indicate that the plug-in system modulates microstructures. In particular, different valence states of Te and Cu were observed in comparisons of Te−Te−RT with the standard doublet of Cu (Figure S5). In addition, compositional analyses using XPS matched the elemental imbalance between the Cu and Te of 1:9, as observed in EDS mapping experiments.

To investigate antibacterial activities, Gram-negative (*E. coli* and ESBL-producing *E. coli*) and Gram-positive (*S. epidermidis* and MRSA) bacteria were treated with different Cu−Te constructs, and comparisons were made with Cu and Te NPs, as shown in Figure 4. MIC and antibacterial efficiencies demonstrate comparable activities of the Cu−Te constructs and Cu NPs, even in MDR strains. Perhaps synergistic effects between Cu^{2+} and TeO$_3$$^{2-}$ or TeO$_4$$^{2-}$ impair membrane functions of bacteria.[47] Approximately 9.7 and 8.1 wt % of Cu and Te were released from Cu−Te constructs after the constructs were incubated in PBS for 24 h at 37 °C, which were observed using inductively coupled plasma−atomic emission spectrometry (ICP−AES). The activities of individual Te NPs against Gram-positive strains were significantly enhanced by incorporating Cu, although MICs for Gram-positive strains were slightly greater than those for Gram-negative microbes in all cases, reflecting the presence of thicker and more complex peptidoglycan layers.[3,48] Lower MICs after Cu−Te−400 and Cu−Te−800 treatments may be related to anisotropic properties (sharp edges or tips) that promote physical damage of bacteria.[49,50] This tendency also matched ROS generation in the Cu−Te construct-treated bacteria (Figure S6), exhibiting greater ROS production from Cu−Te−400 and Cu−Te−800 treatments compared with other configurations. This implies that ROS generation from the treatments may induce a significant influence to suppress the bacterial proliferation. However, differences between the constructs were not significant, suggesting that the combination of Cu and Te is a more critical parameter for enhancing the activity of Te than construct modulation of Cu−Te NPs. To confirm the antimicrobial activities of Cu−Te constructs, the morphologies of Cu−Te-treated bacteria were compared with those of untreated bacteria using SEM analyses (Figure 5). Morphological distortions of treated bacteria were observed with bright spots (Cu−Te constructs), indicating that the antibacterial effects of Cu−Te lead to irreversible cell damage. Corresponding confocal laser scanning microscopy images (insets) of Cu−Te-treated bacteria exhibited no green fluorescent dots (representing viable bacteria) regardless of Cu−Te modulations, again in accordance with comparable MICs and antibacterial efficiencies between Cu−Te constructs.

The toxicity of Cu−Te and the effects of construct modulation on toxicity were assessed in *in vitro* and *in vivo* assays. MTT assays (Figure 6) of Cu−Te-treated HDF and WI-38 cells show concentration dependent effects at 5−200 µg
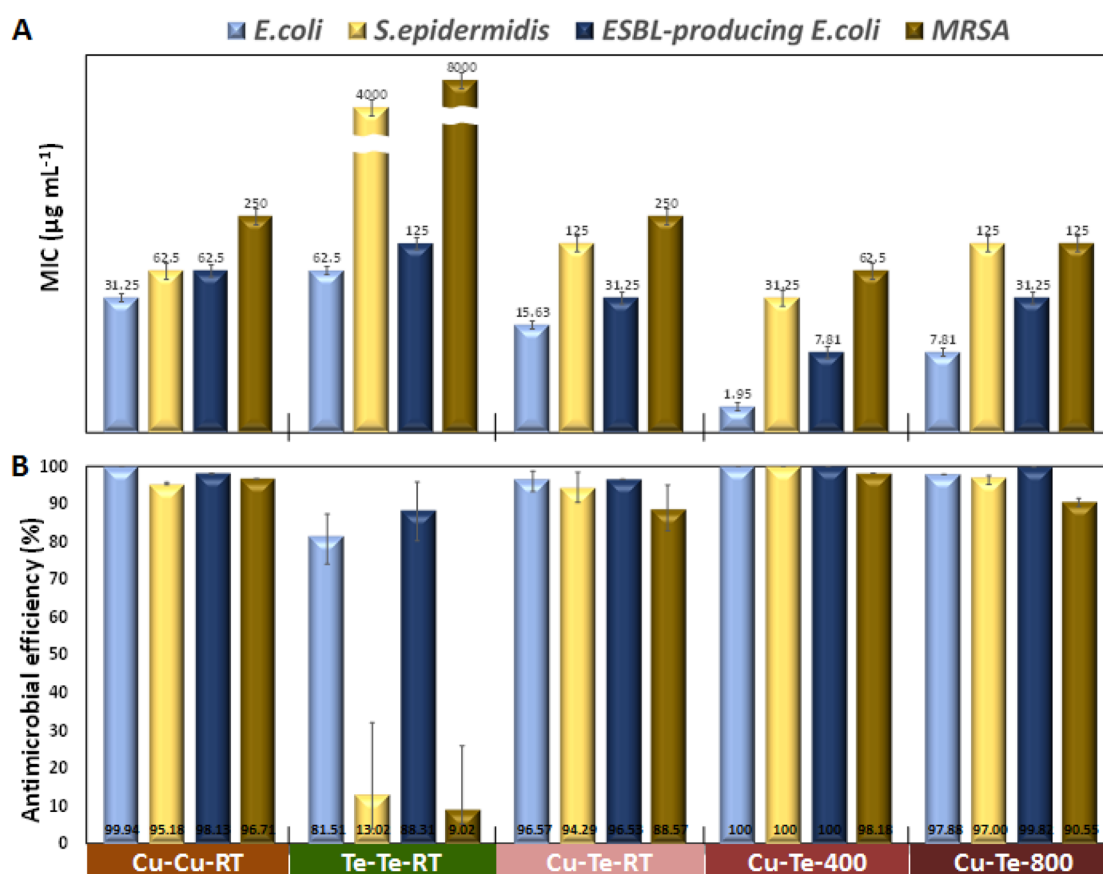
Figure 4. Antibacterial assays in Gram-positive and Gram-negative bacterial strains. (A) Minimum inhibitory concentrations (MICs) and (B) antibacterial activities of Cu−Te constructs and Cu and Te NPs (at RT) were compared in two *Escherichia coli* and two *Staphylococcus* strains. The activities of Cu−Te constructs were more comparable with those of Cu NPs than with those of Te NPs, although differences between the Cu−Te constructs were identified.
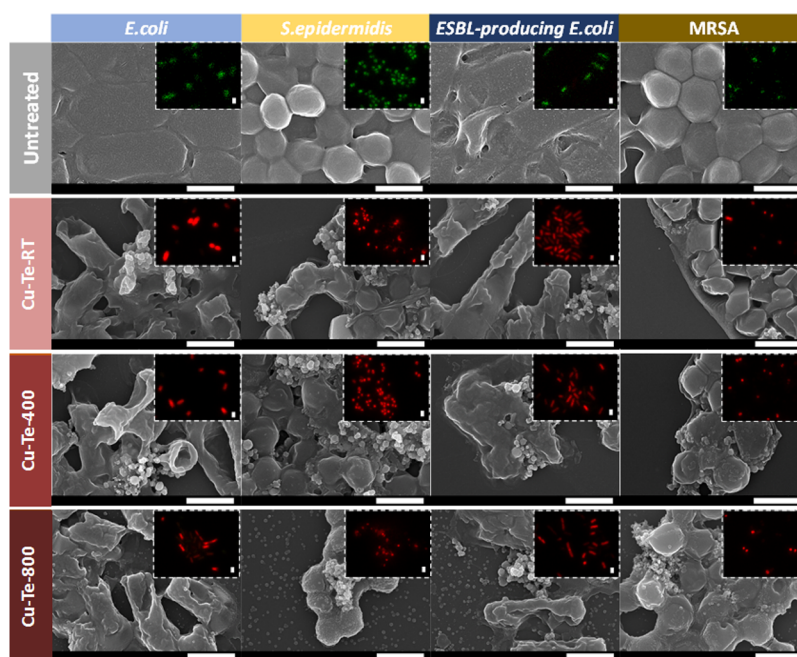

Figure 5. Morphological and staining (inset) analyses of damage to test strains after treatments with different Cu−Te constructs $(30\,\mu g\,mL^{-1})$; comparisons are made with untreated strains. The bright small dots in SEM images show Cu−Te constructs, and the green and red fluorescent dots in confocal laser scanning microscopy images (insets) represent live and dead bacterial cells, respectively. Scale bars, 1 μm.
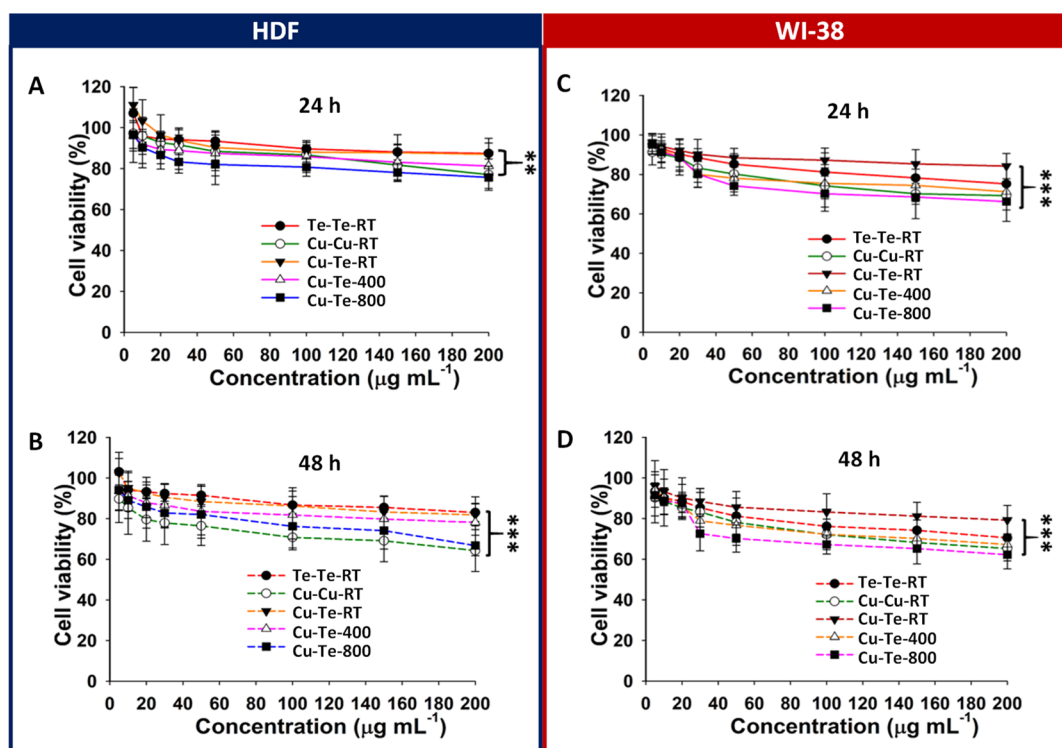
Figure 6. Cytotoxicities of Cu−Te constructs, including individual Te and Cu NPs (at RT) in HDF (A, B) and WI-38 (C, D) cells. Cell viabilities were estimated with different mass concentrations (up to 200 μg mL^{-1}) after 24 and 48 h exposures (**$p < 0.01$ and ***$p < 0.001$).
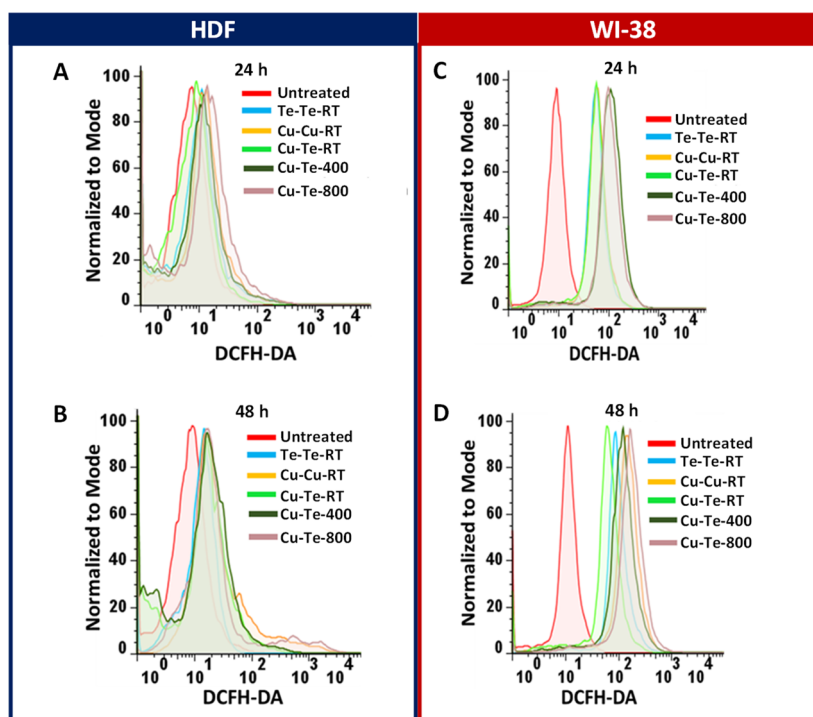

Figure 7. Reactive oxygen species (ROS) generation from Cu−Te (50 μg mL^{-1}) exposures in HDF (A, B) and WI-38 (C, D) cells after 24 and 48 h of incubation; ROS generation from Cu−Te constructs was compared with that from individual Cu and Te NPs.

mL^{-1}. These may be related to the production of free $^1O_2$ and ROS in inorganic nanomaterial-treated mammalian cells.[51] However, cell viability was maintained at approximately 80% even after 24 h treatments with high concentrations (>100 μg mL^{-1}) of NPs, although slight differences between cell lines were observed. No significant changes in the viability at the

higher concentrations might be because of excessive ROS generation that induces senescence process (rather than cell killing) of the cells through oxidative damage to various cellular macromolecules, such as nuclear DNA.[52,53] Cell viabilities after Cu−Te−400 and Cu−Te−800 treatments were similar (more cytotoxic) to those after treatments with individual Cu NPs,
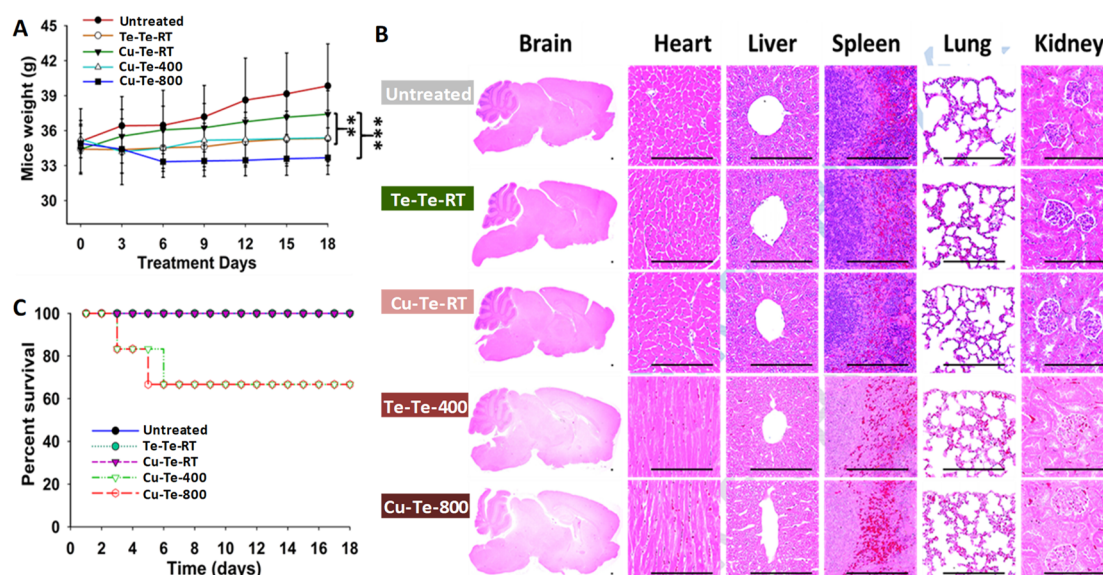
Figure 8. *In vivo* toxicity analyses of Cu−Te constructs; Te NPs (at RT) were included for comparison. (A) Monitored body weights of the Cu−Te-treated ICR mice ($N = 6$ for each case; $**p < 0.01$ and $***p < 0.001$). (B) Organ histopathological profiles of Cu−Te-treated ICR mice after 18 day treatments; mice were intraperitoneally injected with a single 100 mg kg^{-1} dose on day 0. Scale bars, 480 μm. (C) Survival rates of treated mice.

whereas Cu−Te−RT treatments were less toxic, with similar or greater cell viabilities than after treatments with individual Te NPs. These results suggest that the anisotropy of the two constructs further damages fibroblasts. Cu−Te−RT was the least toxic of NPs in both cell lines, indicating that isotropy of its singlet particles minimizes the cytotoxicity of nanoinorganic antibacterials. These cytotoxic profiles of the two cell lines were maintained even for increased incubation times (48 h), suggesting that the elemental imbalance between Cu and Te may be a viable approach for ensuring high biocompatibility of Cu−Te constructs. In DCFH-DA assays, profiles of ROS generation (Figure 7) in Cu−Te (50 μg mL^{-1})-treated cells were in agreement with MTT assay results, and the relatively greater differences between Cu−Te−RT and Cu−Te−400 or Cu−Te−800 constructs were consistent with viability profiles of WI-38 cells (Figure S7). Hence, differences in cytotoxicity between Cu−Te−RT and Cu−Te−400 or Cu−Te−800 might be caused by the differences in ROS production rates and may reflect morphological differences that facilitate differing cytotoxic pathways. Hence, in further experiments we examined morphological changes of Cu−Te (50 μg mL^{-1})-treated cells using optical microscopy over 24 and 48 h treatments (Figure S8). Whereas no significant differences in morphology were observed between Cu−Te-treated and untreated cells, some different shapes were often distributed for Cu−Te−400-, Cu−Te−800-, and Cu−Cu−RT-treated cells, with volume increases and large flat structures from small spindle-fusiforms indicating that cellular senescence was established.[54] Considering the effects of the Te-dominant configuration, these results further support the benefits of construct modulation, because only the anisotropy of chemically nontoxic NPs was associated with senescence and ROS generation, although cellular senescence can also be generated in association with Cu-mediated ROS generation.[54]

The present *in vivo* toxicology measurements included body weights and survival rates and histopathological−histomorphometrical, hematological, and biochemical analyses of mice for the 18 days following single dose treatments with Cu−Te at 100 mg kg^{-1}. No abnormal increases or decreases in body weights were observed in treated mice when compared with untreated mice (Figure 8A), although slight weight losses were detected in Cu−Te−800-treated mice (from 34.9 to 33.6 g over 18 days). Similarly, in pathological analyses, no significant treatment-related histopathological alterations were observed in the major organs of euthanized mice (Figure 8B and Table S1). However, one-third of the Cu−Te−400- and Cu−Te−800-treated mice died during the monitoring period (Figure 8C). These observations may be reflected in our *in vitro* assessments of Cu−Te−400- or Cu−Te−800-treated cells. Specifically, although the toxic effects of the two modulated constructs were not fatal, their biocompatibility was less than that of Cu−Te−RT. According to previous studies for antibacterial validation, in addition, survival rates of antibacterial-treated mice varied from antibacterial materials and testing models,[55−57] although there might be some correlations between the particle anisotropy and cellular (bacterial and animal) damage.[58] Hence, the present toxicological parameters do not firmly represent the state of treated mice, suggesting that monitoring of survival rates may be essential in screens of safe-by-design nanoinorganic antibacterials. To examine the potential for hepatotoxicity of Cu−Te constructs, we performed hematological analyses of treated mice (Table S2). In these experiments, white blood cell, red blood cell, and platelet counts (PLT) were greater in mice treated with Cu−Te−400 and Cu−Te−800 constructs than in untreated mice. Similarly, after treatments with either of the two constructs, mice had elevated hemoglobin (HGB) levels, leading to increases in hematocrit (HCT) percentages. This might be relevant to the unfavorable biocompatibilities of the two constructs, although the percentages remained in the normal range. Ranges of the serum biochemical parameters alkaline phosphatase (ALP), aspartate aminotransferase (AST), alanine aminotransferase (ALT), total protein, total albumin (ALB), blood urea nitrogen (BUN), creatinine (CRE), globulin (GLOB), ALB/GLOB, and BUN/CRE are listed in Table S3. In treated mice, these parameters remained in normal ranges, although differences in ALT/AST, which are indicators of
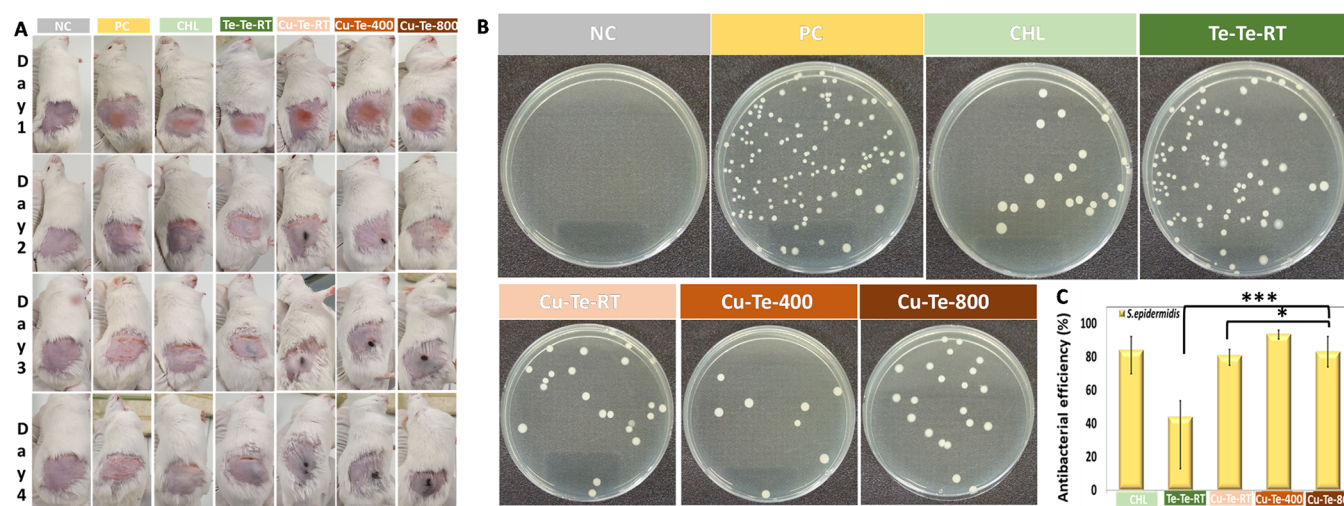
Figure 9. *In vivo* antibacterial activities of Cu−Te constructs; CHL, Te (at RT), NC, and PC after *S. epidermidis* infection of ICR mice. (A) Digital images of the treated mice for 4 days. (B) Digital images of the bacterial colonies grown on agarose gel media after retrieval from the infected skin. The Cu−Te constructs and a commercial broad-spectrum antibiotic CHL exhibited significant inhibitions of *S. epidermidis* growth compared with Te NPs (at RT). (C) Antibacterial efficiencies against *S. epidermidis* infection of ICR mice ($N = 3$ for each case; *$p < 0.01$ and ***$p < 0.001$).

hepatocyte injury or liver fibrosis,[59] and BUN/CRE, which are indicators of impaired kidney function or kidney disease,[60] were observed in comparisons of Cu−Te−400-treated and untreated mice. These results suggest that hematological and biochemical analyses are indicative of the toxicological effects of nano-inorganic antibacterials but need to be consolidated with more reliable analyses using other bioassay data.

According to antibacterial and toxicological assays, modu-lation of Cu−Te constructs affected toxicological screens of observable cytotoxicity, ROS generation, senescence, and survival rates in the presence of Cu−Te−400 and Cu−Te−800 constructs more than in assessments of antibacterial activity, in which no significant differences in MICs and antibacterial efficiency were observed between constructs, even in MDR strains. Hence, efforts to minimize toxicity by controlling compositions and structures may lead to the identification of parameters that confer safe-by-design nanoinorganic constructs in a fast, cost-effective, and highly flexible manner. Such analyses will facilitate timely realization of strong, broadly acting, and safe antibacterials. To this end, our plug-in system and 3 week screening strategy may also offer a platform for more rapid utilization of safe-by-design nanoinorganic antibacterials that can overcome the threats of AMR.

In vivo antibacterial efficacies of Cu−Te constructs against the *S. epidermidis* strain, skin infected wound mice model were further investigated. After skin infection, areas of the infected region were monitored daily (Figure 9A). The infected mice treated with Cu−Te constructs or chloramphenicol (CHL; a commercial broad-spectrum antibiotic) were well-recovered within 4 days of the treatment period, whereas the recovery process was delayed in the Te NPs (at RT) administered group. In the *ex vivo* test, there were no significant differences in *S. epidermidis* growth inhibition (Figure 9B,C) between the Cu−Te construct-treated groups (>80.98% in antibacterial effi-ciency), which were comparable with commercial CHL (84.17%). The significantly lower efficiency (44.12%) from Te NPs (at RT) treatment proved the weak antibacterial activity of Te for Gram-positive bacteria. No significant body weight losses were observed during study period except for the Cu−Te−400-

treated group (Figure S9A), representing that the anisotropy of constituent Cu−Te constructs reduces biosafety. The survival of the treated mice was monitored on a daily basis, and no mice died during the study period (Figure S9B). These *in vivo* results matched the *in vitro* antibacterial and *in vivo* toxicological results, demonstrating the feasibility and reproducibility of the developed plug-in system as a rapid antibacterial screening platform.

CONCLUSIONS

We designed a plug-in system to generate different constructs of nanoinorganic antibacterials and examine antibacterial and toxicological properties in less than 3 weeks (2 days for *in vitro* assays and 18 days for *in vivo* assays). To approach biocompatibility with strong antibacterial activity, we selected Cu, which is an essential nutrient, and Te, which has low toxicity, and generated Cu−Te precursors by ablating Cu and Te rods. Subsequent in-flight modulation was achieved by sintering Cu−Te NPs in a single-pass manner by connecting the spark plasma reactor with a flow heater. By adopting differences in heats of vaporization between Cu and Te, a compositional imbalance (approximately 1:9 of Cu:Te) of precursor Cu−Te NPs was achieved, with higher antibacterial activities than Te alone and lower toxicities than Cu alone. Successively, different heat fluxes from different wall temperatures of the heater induced different degrees of changes in the pore phases of flowing precursor NPs and generated dendritic, spiky, or cubic constructs of Cu−Te within 5 s, demonstrating the convenience and flexibility of the present plug-in system. Antibacterial and toxicological assays showed that the isotropy of constituent Cu−Te constructs is more determining of improved biosafety than of greater antibacterial activity. In particular, fewer sharp edges or low aspect ratios of nanoinorganic constructs may be used to secure higher biosafety, although anisotropic changes may contribute additional physical damage to bacterial cells. The present data suggest that, with convenience and flexibility, our screening platform can provide various precursors with which to build constructs and generate safe-by-design nanoinorganic anti-bacterials in a cost-effective and timely manner.

METHODS

Plug-In Preparation of Different Cu−Te Constructs. Ambient spark ablation was used to supply precursor Cu−Te NPs in a plug-in manner. A bundle of spark microchannels was formed between a Cu rod (3 mm diameter; CU-112564, Nilaco) and a Te rod (6 mm diameter; custom-made, HIGGSLAB) by applying alternating current at high voltage (3.5 kV, 4.0 kHz; BPI-2K, Best Power) as shown in Figure S1A. The gas distance between the rods (Cu, anode; Te, cathode) was maintained at 1 mm, and the rods were placed in a chamber (33 cm^3) under nitrogen gas flow (2 L min^{-1}). Vaporization of the Cu and Te rods was induced by the high temperature of the microchannels, and the vapors were simultaneously condensed into precursor Cu−Te NPs under nitrogen flow at room temperature.

Constructs of the precursor particles were modulated by directly passing them through a tubular flow heater in a single-pass configuration with different wall temperatures [room temperature (RT), 400 °C, and 800 °C] and a residence time of 4.1 s. This process provided different shapes and microstructures of precursor particles from successive heat treatments that induce different thermal behaviors. The resulting particles were collected on a hydrophobic membrane filter (11807-47-N, Sartorius) via mechanical filtration. Particles were precisely injected into buffered saline without purification to secure desired particle concentrations for antibacterial and biosafety assessments.

Characterization. Aerosol size distributions of Cu−Te constructs from heat treatments were measured using SMPS (3936, TSI) immediately after the flow heater with a sampling flow rate of 0.3 L min^{-1}. To analyze shapes, microstructures, and compositions of Cu−Te constructs, the particle-laden flow was injected into an aerosol particle sampler (Ecomesure) with a lacey carbon film-coated copper grid (Graphene Square), which was inserted to directly deposit particles on the grid for TEM (JEM-F200, JEOL) and SEM-EDS (7610F-Plus, JEOL) observations. The resulting particles were also placed on flat substrates for XRD (miniFlex600, Rigaku), XPS (K-Alpha, Thermo Scientific), and Raman spectroscopy (LabRam Aramis, Horiba) analyses, which were used to investigate crystalline and surface structures of the particles. UV−vis spectrophotometry (V-650, Jasco) was used to determine light absorption spectra after dispersing the particles in buffered saline. ICP−AES (OPTIMA 8300, PerkinElmer) was used to identify released Cu and Te ions from Cu−Te constructs after the constructs were incubated in PBS for 24 h, 37 °C, and subsequently separated using a microfiltration kit to extract PBS.

Antibacterial Assay. *Antibacterial Efficiency.* The bacterial strains *E. coli* (ATCC-11775) and *S. epidermidis* (ATCC-14990) and the MDR strains, ESBL-producing *E. coli* (ATCC-25922) and MRSA (ATCC-33591), were treated with Cu−Te constructs to estimate antibacterial efficiencies using a conventional colony counting method (1 × 10^5 CFU mL^{-1} basis) with a UV−vis spectrophotometer operating at a wavelength of 620 nm. For particle treatments, 100 μL aliquots of particle dispersions were added to 2 mL bacterial solutions, and the resulting mixtures were placed in a shaking incubator at 37 °C for 24 h. Subsequently, solutions were diluted with deionized water to ensure desired concentrations for counting of colonies. Solutions were finally spread on agar plates and were cultured at 37 °C for 24 h. Antimicrobial efficacies of Cu−Te constructs were estimated by comparing numbers of CFUs from untreated and treated bacterial cultures.

MIC. MICs of Cu−Te constructs against bacteria were determined using the broth microdilution method. Briefly, bacteria (1 × 10^5 CFU mL^{-1} basis) were seeded onto 96-well microtiter plates (SPL34096, SPL Life Sciences), and particle dispersions in 100 μL aliquots of tryptic soy broth (TSB) with different mass concentrations were added and incubated at 37 °C for 24 h. MICs were eventually determined by analyzing inhibition of bacterial growth at different particle concentrations.

Bacterial Damage. Bacterial damage was examined by observing morphological differences between untreated and treated strains using SEM. Specimens were prepared from cultures of bacteria (1 × 10^5 CFU mL^{-1}) in TSB containing Cu−Te constructs (30 μg mL^{-1}) at 37 °C for 24 h. Treated bacteria were washed and resuspended in deionized

water, and a 5 μL drop of the suspension was then placed on a silicon wafer (Wanxiang). The specimen was dried in ambient air and was finally inserted into a vacuum platinum coater. Damage to particle (30 μg mL^{-1})-treated bacteria (incubated under gentle rotation at 37 °C for 1 h) was further examined by staining bacteria using LIVE/DEAD BacLight bacterial viability kits (L7012, Invitrogen) for confocal laser scanning microscopy (LSM 880, Carl Zeiss) observations.

Toxicity Assay. *Cell Viability.* *In vitro* viability of HDF and WI-38 cells (Korean Cell line Bank) was determined after 24 and 48 h of incubation with Cu−Te constructs using MTT assays. In these experiments, HDF and WI-38 cells were seeded into 96-well plates at 1 × 10^4 cells per well and were exposed to Cu−Te constructs or Te or Cu particles for comparison. MTT reagent (1.25 mg mL^{-1}, 100 μL per well) was added to each well; after 24 or 48 h of incubation, formazan crystals were dissolved in DMSO (cell grade), and absorbance values of solutions were determined using a microplate reader (Multiskan EX, Thermo Scientific) at a wavelength of 570 nm.

Cell Morphology. HDF and WI-38 cells were seeded into 12-well plates at 1 × 10^5 cells per well, were grown overnight, and were then exposed to Cu−Te constructs. Treated cells were washed after 24 or 48 h of incubation, and microscopic images were captured using an inverted microscope (CKX41SF, Olympus).

In Vitro ROS Generation. ROS generation in Cu−Te-treated HDF and WI-38 cells was measured using the oxidation sensitive fluorescent dye DCFH-DA (ab113851, Abcam). Particle-treated (24 or 48 h) cells were washed twice with phosphate-buffered saline (PBS) and were then incubated with DCFH-DA solution (30 μmol L^{-1}) for 30 min in the dark. Cells were washed again with PBS, and fluorescence signals representing ROS generation were observed using a fluorescence microscope. In the case of ROS generation in Cu−Te construct (48 μg mL^{-1})-treated bacteria for 24 h at 37 °C, DCFH-DA-treated bacterial cells were centrifuged for removal of the supernatant. The cells were resuspended in PBS for flow cytometry (BD Biosciences).

In Vivo Toxicity. For *in vivo* toxicity studies, 30 male ICR mice were randomly divided into one control group and four treatment groups of six mice each. Mice were intraperitoneally administered particle constructs in single doses of 100 mg kg^{-1}, and control mice were treated with physiologic saline. The mice were weighed and assessed for behavioral changes every 3 days after injections and were sacrificed after 18 days.

Histopathological Analysis. For histopathological analyses, brain, heart, liver, spleen, lung, and kidney tissues were excised from all animals, fixed in 10% neutral buffered formalin, embedded in paraffin using an automated tissue processor (Shandon Citadel 2000, Thermo Scientific), and sectioned at 3−4 μm using a microtome (RM2255, Leica Biosystems). Sections were then stained with H&E and were observed using light microscopy (Model Eclipse 80*i*, Nikon).

Biochemical Blood Analysis. Based on a standard cardiac puncture collection technique, blood was drawn from anesthetized mice for hematology analyses. For blood analysis, 1 mL aliquots of blood were collected from treated mice on day 18 and were centrifuged at 3000 rpm for 15 min at 4 °C to obtain serum. The hematological parameters such as white blood cells, red blood cells, HGB, HCT, and others were examined. Moreover, serum levels of ALP and AST were analyzed to evaluate the effects of the treatments on liver function. BUN and CRE levels were analyzed to examine nephrotoxicity.

In Vivo Antibacterial Assay. Male ICR mice (30−40 g; 6 weeks of age) were kept for 1 week to be acclimatized in individually ventilated cages (specific pathogen-free state) at 22 ± 2 °C and 40−60% relative humidity under a strict 12/12 h light/dark cycle prior to the investigation. Skin infection of ICR mice with *S. epidermidis* was performed as described previously.[61−63] Briefly, mice were anesthetized (ketamine/xylazine cocktail; 0.1 mL/20 g), disinfected with ethanol (70%), shaved dorsally (about 3 cm^2), tape stripped on the shaved area (2.5 cm^2), injected subcutaneously with 200 μL of *S. epidermidis* at a concentration of 1 × 10^7 CFU mL^{-1}, and kept overnight to infect the mice. The infected mice were then randomized into six groups, with three mice in each group. The infected six groups were treated subcutaneously with Cu−Te constructs or Te NPs (at RT) at a dose of 25 mg kg^{-1}, including 200 μL of normal saline (positive control; PC) or

CHL, at a 24 h interval for 3 days. One group was left uninfected and untreated as a negative control (NC). The mice were monitored for the development of skin abscesses and lesions characterized by swelling, redness, and other inflammatory reactions throughout the study period. At day 4 of the treatments, mice were sacrificed; 300 mg of wound (~1 cm^2) was removed and homogenized with 3 mL of phosphate buffer. A 10 μL portion of homogenates was finally taken to carry out a pour plate technique to determine the CFU of alive bacteria and to compare it with other groups.

Statistical Analysis. Differences between treatments were identified using one-way ANOVA or Student's *t*-tests, and levels of significance are presented for each result.

Ethical Statement. All animal procedures were performed in accordance with the Guidelines for Care and Use of Laboratory Animals of Yeungnam University and were approved by the Institutional Animal Ethics Committee of Yeungnam University.

ASSOCIATED CONTENT

ⓢ Supporting Information

The Supporting Information is available free of charge on the ACS Publications website at DOI: 10.1021/acsnano.9b04939.

> Digital image of plug-in system; aerosol size distributions; EDS and Raman analyses; XRD profiles of Cu−Te constructs from 400 and 800 °C; UV−vis absorption spectra and digital images of Cu−Te dispersions; core Te and Cu XPS spectra; ROS generation in Cu−Te-treated bacterial or HDF and WI-38 cells; optical microscope images of Cu−Te-treated HDF and WI-38 cells; and summaries of histopathological−histomorphometrical, hematological, and biochemical analyses of Cu−Te-treated ICR mice (PDF)

AUTHOR INFORMATION

Corresponding Authors
*E-mail: hwangjh@yonsei.ac.kr. (J.H.)
*E-mail: jongohkim@yu.ac.kr. (J.O.K.)
*E-mail: postjb@yu.ac.kr. (J.H.B.)

ORCID 🄾
Jungho Hwang: 0000-0002-0304-7360
Jong Oh Kim: 0000-0002-4929-851X
Jeong Hoon Byeon: 0000-0003-0903-7128

Author Contributions
‖M.G. and D.H.P. contributed equally to this work.

Notes
The authors declare no competing financial interest.

REFERENCES

(1) Van Giau, V.; An, S. S. A.; Hulme, J. Recent Advances in the Treatment of Pathogenic Infections Using Antibiotics and Nano-Drug Delivery Vehicles. *Drug Des., Dev. Ther.* **2019**, *13*, 327−343.

(2) Brown, C. D.; Cruz, D. M.; Roy, A. K.; Webster, T. J. Synthesis and Characterization of PVP-Coated Tellurium Nanorods and Their Antibacterial and Anticancer Properties. *J. Nanopart. Res.* **2018**, *20*, 254.

(3) Chang, H.-Y.; Cang, J.; Roy, P.; Chang, H.-T.; Huang, Y.-C.; Huang, C.-C. Synthesis and Antimicrobial Activity of Gold/Silver−Tellurium Nanostructures. *ACS Appl. Mater. Interfaces* **2014**, *6*, 8305−8312.

(4) Ali, S. R.; Pandit, S.; De, M. 2D-MoS$_2$-Based β-Lactamase Inhibitor for Combination Therapy against Drug-Resistant Bacteria. *ACS Appl. Bio Mater.* **2018**, *1*, 967−974.

(5) Koluman, A.; Dikici, A. Antimicrobial Resistance of Emerging Foodborne Pathogens: Status Quo and Global Trends. *Crit. Rev. Microbiol.* **2013**, *39*, 57−69.

(6) Roope, L. S. J.; Smith, R. D.; Pouwels, K. B.; Buchanan, J.; Abel, L.; Eibich, P.; Butler, C. C.; Tan, P. S.; Walker, A. S.; Robotham, J. V.; Wordsworth, S. The Challenge of Antimicrobial Resistance: What Economics Can Contribute. *Science* **2019**, *364*, No. eaau4679.

(7) Abo Elsoud, M. M.; Al-Hagar, O. E. A.; Abdelkhalek, E. S.; Sidkey, N. M. Synthesis and Investigations on Tellurium Myconanoparticles. *Biotechnol. Rep.* **2018**, *18*, No. e00247.

(8) Sosedova, L. M.; Rukavishnikov, V. S.; Sukhov, B. G.; Borovskii, G. B.; Titov, E. A.; Novikov, M. A.; Vokina, V. A.; Yakimova, N. L.; Lesnichaya, M. V.; Kon'kova, T. V.; Borovskaya, M. K.; Graskova, I. A.; Perfil'eva, A. I.; Trofimov, B. A. Synthesis of Chalcogen-Containing Nanocomposites of Selenium and Tellurium with Arabinogalactan and a Study of Their Toxic and Antimicrobial Properties. *Nanotechnol. Russ.* **2018**, *13*, 290−294.

(9) Ding, X.; Wang, A.; Tong, W.; Xu, F.-J. Biodegradable Antibacterial Polymeric Nanosystems: A New Hope to Cope with Multidrug-Resistance Bacteria. *Small* **2019**, *15*, 1900999.

(10) Hochella, M. F., Jr.; Mogk, D. W.; Ranville, J.; Allen, I. C.; Luther, G. W.; Marr, L. C.; McGrail, B. P.; Murayama, M.; Qafoku, N. P.; Rosso, K. M.; Sahai, N.; Schroeder, P. A.; Vikesland, P.; Westerhoff, P.; Yang, Y. Natural, Incidental, and Engineered Nanomaterials and Their Impacts on the Earth System. *Science* **2019**, *363*, No. eaau8299.

(11) Zonaro, E.; Lampis, S.; Turner, R. J.; Qazi, S. J. S.; Vallini, G. Biogenic Selenium and Tellurium Nanoparticles Synthesized by Environmental Microbial Isolates Efficaciously Inhibit Bacterial Planktonic Cultures and Biofilms. *Front. Microbiol.* **2015**, *6*, 584.

(12) Guisbiers, G.; Mimun, L. C.; Mendoza-Cruz, R.; Nash, K. L. Synthesis of Tunable Tellurium Nanoparticles. *Semicond. Sci. Technol.* **2017**, *32*, No. 04LT01.

(13) Ahmed, K. B. A.; Raman, T.; Veerappan, A. Future Prospects of Antibacterial Metal Nanoparticles as Enzyme Inhibitor. *Mater. Sci. Eng., C* **2016**, *68*, 939−947.

(14) Medina Cruz, D.; Tien-Street, W.; Zhang, B.; Huang, X.; Crua, A. V.; Nieto-Argüello, A.; Cholula-Díaz, J. L.; Martínez, L.; Huttel, Y.; González, M. U.; García-Martín, J. M.; Webster, T. J. Citric Juice-Mediated Synthesis of Tellurium Nanoparticles with Antimicrobial and Anticancer Properties. *Green Chem.* **2019**, *21*, 1982−1998.

(15) Borghese, R.; Brucale, M.; Fortunato, G.; Lanzi, M.; Mezzi, A.; Valle, F.; Cavallini, M.; Zannoni, D. Extracellular Production of Tellurium Nanoparticles by the Photosynthetic Bacterium *Rhodobacter Capsulatus*. *J. Hazard. Mater.* **2016**, *309*, 202−209.

(16) Presentato, A.; Piacenza, E.; Darbandi, A.; Anikovskiy, M.; Cappelletti, M.; Zannoni, D.; Turner, R. J. Assembly, Growth and Conductive Properties of Tellurium Nanorods Produced by *Rhodococcus Aetherivorans* BCP1. *Sci. Rep.* **2018**, *8*, 3923.

(17) Pugin, B.; Cornejo, F. A.; Muñoz-Díaz, P.; Muñoz-Villagrán, C. M.; Bargas-Pérez, J. I.; Arenas, F. A.; Vásquez, C. C. Glutathione Reductase-Mediated Synthesis of Tellurium-Containing Nanostructures Exhibiting Antibacterial Properties. *Appl. Environ. Microbiol.* **2014**, *80*, 7061−7070.

(18) Ramesh, S.; Kim, H. S.; Msolli, S.; Rengaraj, A. K.; Huh, Y. S.; Kim, J.-H. Rod-Like Structure of Cotton Cellulose/Polyvinyl Alcohol/Tellurium Dioxide (TeO$_2$) Hybrid Nanocomposite and Antimicrobial Properties. *Polym.-Plast. Technol. Eng.* **2018**, *57*, 1131−1138.

(19) Feng, J.; Guo, X.; Ramlawi, N.; Pfeiffer, T. V.; Geutjens, R.; Basak, S.; Nirschl, H.; Biskos, G.; Zandbergen, H. W.; Schmidt-Ott, A. Green Manufacturing of Metallic Nanoparticles: A Facile and Universal Approach to Scaling Up. *J. Mater. Chem. A* **2016**, *4*, 11222−11227.

(20) Park, D. H.; Joe, Y. H.; Hwang, J.; Byeon, J. H. Evaporation-Condensation in the Presence of Unipolar Ionic Flow for Solvent-Free Production of Ultrasmall Antibacterial Particles. *Chem. Eng. J.* **2020**, *381*, 122639.

(21) Byeon, J. H. Rapid Green Assembly of Antimicrobial Nanobunches. *Sci. Rep.* **2016**, *6*, 27006.

(22) Tsantilis, S.; Pratsinis, S. E. Evolution of Primary and Aggregate Particle-Size Distributions by Coagulation and Sintering. *AIChE J.* **2000**, *46*, 407−415.

(23) Byeon, J. H.; Park, J. H.; Peters, T. M.; Roberts, J. T. Reducing the Cytotoxicity of Inhalable Engineered Nanoparticles *via In Situ* Passivation with Biocompatible Materials. *J. Hazard. Mater.* **2015**, *292*, 118−125.

(24) Byeon, J. H.; Kim, J.-W. Production of Carbonaceous Nanostructures from a Silver−Carbon Ambient Spark. *Appl. Phys. Lett.* **2010**, *96*, 153102.

(25) Coble, R. L. Sintering Crystalline Solids. II. Experimental Test of Diffusion Models in Powder Compacts. *J. Appl. Phys.* **1961**, *32*, 793−799.

(26) Chatterjee, A. K.; Chakraborty, R.; Basu, T. Mechanism of Antibacterial Activity of Copper Nanoparticles. *Nanotechnology* **2014**, *25*, 135101.

(27) Balela, M. D. L.; Amores, K. L. S. Electroless Deposition of Copper Nanoparticle for Antimicrobial Coating. *Mater. Chem. Phys.* **2019**, *225*, 393−398.

(28) Molina-Quiroz, R. C.; Muñoz-Villagrán, C. M.; de la Torre, E.; Tantaleán, J. C.; Vásquez, C. C.; Pérez-Donoso, J. M. Enhancing the Antibiotic Antibacterial Effect by Sub Lethal Tellurite Concentrations: Tellurite and Cefotaxime Act Synergistically in *Escherichia coli*. *PLoS One* **2012**, *7*, No. e35452.

(29) Zare, B.; Faramarzi, M. A.; Sepehrizadeh, Z.; Shakibaie, M.; Rezaie, S.; Shahverdi, A. R. Biosynthesis and Recovery of Rod-Shaped Tellurium Nanoparticles and Their Bactericidal Activity. *Mater. Res. Bull.* **2012**, *47*, 3719−3725.

(30) Shakibaie, M.; Adeli-Sardou, M.; Mohammadi-Khorsand, T.; Zeydabadi-Nejad, M.; Amirafzali, E.; Amirpour-Rostami, S.; Ameri, A.; Forootanfar, H. Antimicrobial and Antioxidant Activity of the Biologically Synthesized Tellurium Nanorods: A Preliminary *In Vitro* Study. *Iran. J. Biotechnol.* **2017**, *15*, No. 268.

(31) Cholewińska, E.; Ognik, K.; Fotschki, B.; Zduńczyk, Z.; Juśkiewicz, J. Comparison of the Effect of Dietary Copper Nanoparticles and One Copper (II) Salt on the Copper Biodistribution and Gastrointestinal and Hepatic Morphology and Function in a Rat Model. *PLoS One* **2018**, *13*, No. e0197083.

(32) Matharu, R. K.; Charani, Z.; Ciric, L.; Illangakoon, U. E.; Edirisinghe, M. Antimicrobial Activity of Tellurium-Loaded Polymeric Fiber Meshes. *J. Appl. Polym. Sci.* **2018**, *135*, 46368.

(33) Chou, T.-M.; Ke, Y.-Y.; Tsao, Y.-H.; Li, Y.-C.; Lin, Z.-H. Fabrication of Te and Te−Au Nanowires-Based Carbon Fiber Fabrics for Antibacterial Applications. *Int. J. Environ. Res. Public Health* **2016**, *13*, 202.

(34) Zhong, C. L.; Qin, B. Y.; Xie, X. Y.; Bai, Y. Antioxidant and Antimicrobial Activity of Tellurium Dioxide. *J. Nano Res.* **2013**, *25*, 8−15.

(35) Taylor, A. Biochemistry of Tellurium. *Biol. Trace Elem. Res.* **1996**, *55*, 231−239.

(36) Lin, Z. H.; Lee, C. H.; Chang, H. Y.; Chang, H. T. Antibacterial Activities of Tellurium Nanomaterials. *Chem. - Asian J.* **2012**, *7*, 930−934.

(37) Lee, I.-C.; Ko, J.-W.; Park, S.-H.; Lim, J.-O.; Shin, I.-S.; Moon, C.; Kim, S.-H.; Heo, J.-D.; Kim, J.-C. Comparative Toxicity and Biodistribution of Copper Nanoparticles and Cupric Ions in Rats. *Int. J. Nanomed.* **2016**, *11*, 2883−2900.

(38) Mirjani, R.; Faramarzi, M. A.; Sharifzadeh, M.; Setayesh, N.; Khoshayand, M. R.; Shahverdi, A. R. Biosynthesis of Tellerium Nanoparticles by *Lactobacillus Plantarum* and the Effect of Nanoparticle-Enriched Probiotics on the Lipid Profiles of Mice. *IET Nanobiotechnol.* **2015**, *9*, 300−305.

(39) Vij, P.; Hardej, D. Evaluation of Tellurium Toxicity in Transformed and Non-Transformed Human Colon Cells. *Environ. Toxicol. Pharmacol.* **2012**, *34*, 768−782.

(40) Ma, C.; Yan, J.; Huang, Y.; Wang, C.; Yang, G. The Optical Duality of Tellurium Nanoparticles for Broadband Solar Energy Harvesting and Efficient Photothermal Conversion. *Sci. Adv.* **2018**, *4*, No. eaas9894.

(41) Kim, J. E.; Nam, J. H.; Cho, J. Y.; Kim, K. S.; Hwang, D. Y. Annual Tendency of Research Papers Used ICR Mice as Experimental Animals in Biomedical Research Fields. *Lab. Anim. Res.* **2017**, *33*, 171−178.

(42) Feng, J.; Biskos, G.; Schmidt-Ott, A. Toward Industrial Scale Synthesis of Ultrapure Singlet Nanoparticles with Controllable Sizes in a Continuous Gas-Phase Processes. *Sci. Rep.* **2015**, *5*, 15788.

(43) Goudeli, E.; Eggersdorfer, M. L.; Pratsinis, S. E. Coagulation of Agglomerates Consisting of Polydisperse Primary Particles. *Langmuir* **2016**, *32*, 9276−9285.

(44) Li, H.; Brescia, R.; Povia, M.; Prato, M.; Bertoni, G.; Manna, L.; Moreels, I. Synthesis of Uniform Disk-Shaped Copper Telluride Nanocrystals and Cation Exchange to Cadmium Telluride Quantum Disks with Stable Red Emission. *J. Am. Chem. Soc.* **2013**, *135*, 12270−12278.

(45) Xi, G.; Peng, Y.; Yu, W.; Qian, Y. Synthesis, Characterization, and Growth Mechanism of Tellurium Nanotubes. *Cryst. Growth Des.* **2005**, *5*, 325−328.

(46) Mousavi-Kamazani, M.; Rahmatolahzadeh, R.; Shobeiri, S. A.; Beshkar, F. Sonochemical Synthesis, Formation Mechanism, and Solar Cell Application of Tellurium Nanoparticles. *Ultrason. Sonochem.* **2017**, *39*, 233−239.

(47) Lemire, J. A.; Harrison, J. J.; Turner, R. J. Antimicrobial Activity of Metals: Mechanisms, Molecular Targets and Applications. *Nat. Rev. Microbiol.* **2013**, *11*, 371−384.

(48) Kim, J. S.; Kuk, E.; Yu, K. N.; Kim, J.-H.; Park, S. J.; Lee, H. J.; Kim, S. H.; Park, Y. K.; Park, Y. H.; Hwang, C.-Y.; Kim, Y.-K.; Lee, Y.-S.; Jeong, D. H.; Cho, M.-H. Antimicrobial Effects of Silver Nanoparticles. *Nanomedicine* **2007**, *3*, 95−101.

(49) Hu, H.; Siu, V. S.; Gifford, S. M.; Kim, S.; Lu, M.; Meyer, P.; Stolovitzky, G. A. Bio-Inspired Silicon Nanospikes Fabricated by Metal-Assisted Chemical Etching for Antibacterial Surfaces. *Appl. Phys. Lett.* **2017**, *111*, 253701.

(50) Tripathy, A.; Sreedharan, S.; Bhaskarla, C.; Majumdar, S.; Peneti, S. K.; Nandi, D.; Sen, P. Enhancing the Bactericidal Efficacy of Nanostructured Multifunctional Surface Using an Ultrathin Metal Coating. *Langmuir* **2017**, *33*, 12569−12579.

(51) Henson, T. E.; Navratilova, J.; Tennant, A. H.; Bradham, K. D.; Rogers, K. R.; Hughes, M. F. *In Vitro* Intestinal Toxicity of Copper Oxide Nanoparticles in Rat and Human Cell Models. *Nanotoxicology* **2019**, *13*, 795−811.

(52) Nita, M.; Grzybowski, A. The Role of the Reactive Oxygen Species and Oxidative Stress in the Pathomechanism of the Age-Related Ocular Diseases and Other Pathologies of the Anterior and Posterior Eye Segments in Adults. *Oxid. Med. Cell. Longevity* **2016**, *2016*, 3164734.

(53) Pole, A.; Dimri, M.; Dimri, G. P. Oxidative Stress, Cellular Senescence and Ageing. *AIMS Mol. Sci.* **2016**, *3*, 300−324.

(54) Matos, L.; Gouveia, A.; Almeida, H. Copper Ability to Induce Premature Senescence in Human Fibroblasts. *Age (Dordr).* **2012**, *34*, 783−794.

(55) Brunetti, J.; Falciani, C.; Roscia, G.; Pollini, S.; Bindi, S.; Scali, S.; Arrieta, U. C.; Gómez-Vallejo, V.; Quercini, L.; Ibba, E.; Prato, M.; Rossolini, G. M.; Llop, J.; Bracci, L.; Pini, A. *In Vitro* and *In Vivo* Efficacy, Toxicity, Bio-Distribution and Resistance Selection of a Novel Antibacterial Drug Candidate. *Sci. Rep.* **2016**, *6*, 26077.

(56) Gorr, S.-U.; Flory, C. M.; Schumacher, R. J. *In Vivo* Activity and Low Toxicity of the Second-Generation Antimicrobial Peptide DGL13K. *PLoS One* **2019**, *14*, No. e0216669.

(57) Johari, S. A.; Mohtar, M.; Mohamad, S. A. S.; Mohammat, M. F.; Sahdan, R.; Mohamed, A.; Ridhwan, M. J. M. *In Vitro* Evaluations and *In Vivo* Toxicity and Efficacy Studies of MFM501 against MRSA. *BioMed Res. Int.* **2017**, *2017*, 8032865.

(58) Wang, L.; Chen, Y.; Lin, H. Y.; Hou, Y.-T.; Yang, L.-C.; Sun, A. Y.; Liu, J.-Y.; Chang, C.-W.; Wan, D. Near-IR-Absorbing Gold Nanoframes with Enhanced Physiological Stability and Improved Biocompatibility for *In Vivo* Biomedical Applications. *ACS Appl. Mater. Interfaces* **2017**, *9*, 3873−3884.

(59) Hakkak, R.; Gauss, H. C.; Bell, A.; Korourian, S. Short-Term Soy Protein Isolate Feeding Prevents Liver Steatosis and Reduces Serum ALT and AST Levels in Obese Female Zucker Rats. *Biomedicines* **2018**, *6*, 55.

(60) Xie, Y.; Bowe, B.; Li, T.; Xian, H.; Yan, Y.; Al-Aly, Z. Higher Blood Urea Nitrogen is Associated with Increased Risk of Incident Diabetes Mellitus. *Kidney Int.* **2018**, *93*, 741−752.

(61) Escárcega-González, C. E.; Garza-Cervantes, J. A.; Vázquez-Rodríguez, A.; Montelongo-Peralta, L. Z.; Treviño-González, M. T.; Castro, E. D. B.; Saucedo-Salazar, E. M.; Morales, R. M. C.; Soto, D. I. R.; González, F. M. T.; Rosales, J. L. C.; Cruz, R. V.; Morones-Ramírez, J. R. *In Vivo* Antimicrobial Activity of Silver Nanoparticles Produced *via* a Green Chemistry Synthesis Using *Acacia rigidula* as a Reducing and Capping Agent. *Int. J. Nanomed.* **2018**, *13*, 2349−2363.

(62) Le, K. Y.; Villaruz, A. E.; Zheng, Y.; He, L.; Fisher, E. L.; Nguyen, T. H.; Ho, T. V.; Yeh, A. J.; Joo, H.-S.; Cheung, G. Y. C.; Otto, M. Role of Phenol-Soluble Modulins in *Staphylococcus epidermidis* Biofilm Formation and Infection of Indwelling Medical Devices. *J. Mol. Biol.* **2019**, *431*, 3015−3027.

(63) Kugelberg, E.; Norström, T.; Petersen, T. K.; Duvold, T.; Andersson, D. I.; Hughes, D. Establishment of a Superficial Skin Infection Model in Mice by Using *Staphylococcus aureus* and *Streptococcus pyogenes*. *Antimicrob. Agents Chemother.* **2005**, *49*, 3435−3441.